RESEARCH PAPER

Understanding the formation of "false friends" (hidden lack of fusion defects) in laser beam welding by means of high-speed synchrotron X-ray imaging

K. Schricker[1] · C. Diegel[1] · L. Schmidt[1] · M. Seibold[1] · H. Friedmann[1] · F. Fröhlich[1] · S. Eichler[1] · Y. Chen[2,3,4] · H. Requardt[2] · A. Rack[2] · J. P. Bergmann[1]

Abstract

This paper provides a fundamental understanding of "false friend" formation, i.e., hidden defects associated with lack of fusion, using an experimental setup that allowed an insight into the processing zone based on high-speed synchrotron X-ray imaging. The setup enabled the welding of a lap joint of AISI 304 high-alloy steel sheets (X5CrNi18-10/1.4301), with the ability to adjust different gap heights between top and bottom sheet (up to 0.20 mm) and to acquire high-speed X-ray images at 100 kHz simultaneously with the welding process. On this basis, a time-resolved description of the "false friend" formation can be provided by visualizing the interaction between keyhole and melt pool during laser welding and solidification processes within the gap area. The bridgeability of the gap was limited due to the gap height and insufficient melt supply leading to the solidification of the bridge. The distance between the solidified bridge and the keyhole increased with time, while the keyhole and melt pool dynamics initiated the formation of new melt bridges whose stability was defined by melt flow conditions, surface tension, and gap heights. The alternating formation and solidification of melt bridges resulted in entrapped areas of lacking fusion within the weld, i.e., "false friends." Finally, based on the results of this study, a model concept is presented that concludes the main mechanisms of "false friend" formation.

Keywords Laser beam welding · X-ray imaging · Synchrotron · Lap joint · High-alloy steel · False friend · Lack of fusion · Weld defect · In situ

1 Introduction

Laser beam welding enables high processing speeds due to its non-contact energy input, high power density, and high degree of automation [1]. This leads to a high industrial relevance of laser beam welding for numerous applications, such as in the automotive industry [2], domestic appliances [3], and energy sector [4]. For many of these applications, such as bipolar plates for fuel cells [5], high-alloy steels are employed on the one hand due to their properties, e.g., corrosion resistance [6]. On the other hand, lap joints are often used because of their ability to bridge manufacturing tolerances, thereby reducing the need and cost for fixtures and part preparation [7].

When welding lap joints, particular attention must be paid to the formation of hidden defects associated with lack of fusion, known as "false friends" [8]. As a result, both the mechanical properties of the weld and the tightness or electrical conductivity can be negatively affected which is highly relevant for different applications, e.g., fuel cells [9]. These defects are hidden within the weld and cannot be visually detected from the surface or root position [10]. "False friends" usually occur at the interface between the two sheets and represent a separation of the fusion zone [11]

✉ K. Schricker
klaus.schricker@tu-ilmenau.de

1   Production Technology Group, Technische Universität Ilmenau, Ilmenau, Germany

2   Structure of Materials Group – ID19, ESRF – The European Synchrotron, Grenoble, France

3   Department of Materials, The University of Manchester, Manchester, Great Britain

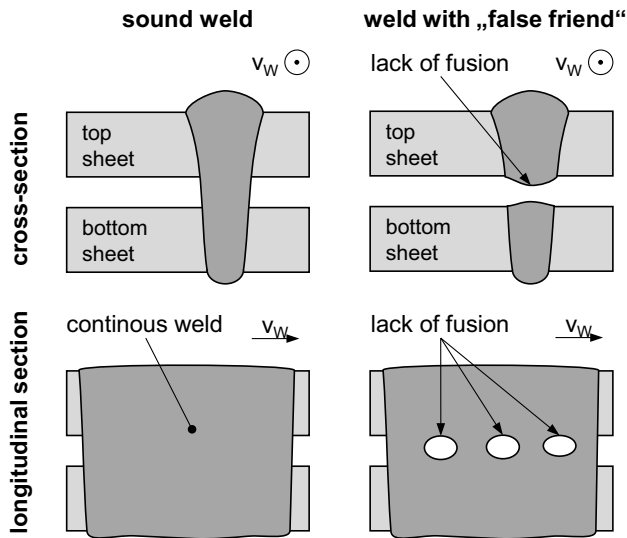4   School of Engineering, RMIT University, Melbourne, Australia

Fig. 1 Welding with gap in overlap joint: schematic cross-section of a regular weld seam and a weld with a "false friend"
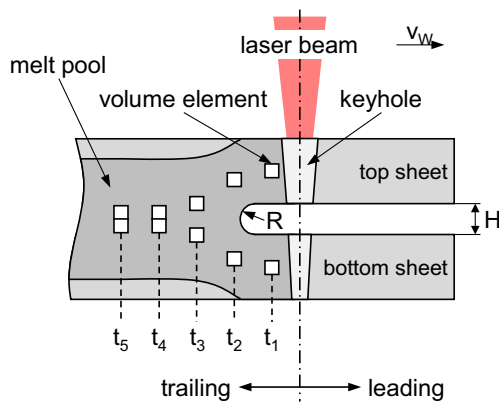

Fig. 2 Melt flow for gap bridging based on [11]

(see Fig. 1). Consequently, the weld between top and bottom sheets are separated in certain areas [11]. The gap height, when the melt is no longer able to bridge the gap, has been identified as the critical factor in the occurrence of "false friends" [12]. The ability of melt to bridge the gap is presumed to be affected by viscosity and surface tension, cohesive and weight forces, melt flow conditions, sheet thickness, gap height, and welding speed leading to two melt pools that are expected to coalesce behind the keyhole [11].

Figure 2 shows the model concept of [11] for different time steps (t_1 to t_5) and exemplary volume elements without taking turbulences into consideration for forming a melt bridge trailing to welding direction. The volume elements from top and bottom sheet are transported backwards and form a common melt pool trailing to the keyhole.

When a certain gap height H is exceeded, the melt is no longer able to bridge the gap, and melt ejections or spatters are required to re-establish a melt bridge, as discussed by [11]. This aspect is particularly interesting because "false friends" usually do not represent a continuous separation of the two sheets in the lap joint but are trapped in the weld and occur repeatedly as shown in [13] (see Fig. 1). Such effects, i.e., melt ejections and spatters, are mainly caused due to the interaction of metal vapor from the keyhole with the melt pool [14]. The underlying phenomena take place inside the material and are therefore not directly observable. The use of high-energy, brilliant synchrotron radiation enables high temporal and spatial resolution of the X-ray imaging [15, 16] providing the opportunity to gain insight into the behavior of the keyhole and its interaction with the melt pool. These capabilities have been proven for laser welding of different materials at high acquisition rates, e.g., copper up to 20 kHz [17], aluminum up to approx. 28 kHz [18], or titanium alloys between 40 kHz [19] up to approx. 1 MHz [20]. In addition to the characteristics and energy of the synchrotron radiation, the irradiated sample thickness, the density, and the addressed size of the region of interest have a significant impact on the achievable frame rates.

It can be stated that systematic knowledge that consistently describes the formation of "false friends" and their correlation to the aforementioned factors is not yet fully understood, i.e., formation and stability of bridging the gap by the melt pool and the effect of interactions between keyhole and melt pool. However, there is some insight into melt bridge behavior in the area of capillary bridges, i.e., the formation of a liquid film between two bodies retained by surface tension [21]. It is known that the dimensionless bond number (see Eq. 1) can be utilized for describing the stability of the capillary bridge considering density difference to the surrounding atmosphere ρ, gravitational acceleration g, and melt bridge Radius R and surface tension σ [22]. The considerations usually require equilibrium conditions [22] which, of course, do not apply in the welding process. Nevertheless, the applicability of Young's equation, among others, which is subject to comparable restrictions, shows a good informative value for the wetting behavior in joining processes [23]. The material properties can be assumed to be constant for simplicity, as is already known from various dimensionless numbers utilized to describe laser welding processes [24, 25]. Therefore, the bond number may allow a simplified but still coupled consideration of the melt bridge geometry in terms of its radius (see R in Fig. 2) and the surface tension σ of the melt as it can be interpreted physically as the ratio of volumetric force to surface tension force.

$$Bo = \frac{\rho g R^2}{\sigma} \tag{1}$$

This paper addresses the formation of "false friends" in laser beam welding based on a simplified specimen geometry utilizing high-speed synchrotron X-ray imaging. The setup enables the observation of phenomena inside the material, i.e., keyhole and melt pool interaction, with high temporal and spatial resolution. Therefore, small sample thicknesses are be addressed for welding while avoiding significant heat accumulation in order to achieve high acquisition rates of 100 kHz. The selective adjustment of different gap heights enforces the occurrence of false friends and allows the parallel recording of the associated phenomena. The interaction between the keyhole and the melt pool, the behavior, and the melt bridges, as well as the solidification processes within the gap allow an in-depth description of the present mechanisms leading to "false friends."

2 Materials and methods

2.1 Laser welding setup

The welding process was performed using an IPG YLM-450/4500-QCW fiber laser and a stationary IPG D30 laser welding head. The laser beam source was used in cw-mode for a continuous power output. The beam power was measured by COHERENT PowerMax Pro-HP showing that an output power of 380 W was used for carrying out the welds in cw-mode. Table 1 summarizes the relevant parameters of the laser welding setup.

2.2 High-speed synchrotron X-ray imaging

The high recording frequency of the synchrotron X-ray imaging allowed the systematic study of the formation of "false friends" depending on keyhole and melt pool behavior. For this purpose, a top sheet with a constant thickness of 0.5 mm was clamped to a bottom sheet (see Fig. 3). The top sheet was wire cut from a rolled plate of 0.5 mm thickness to minimize the effect of the cutting process on distortion present before the welding process. The rolling
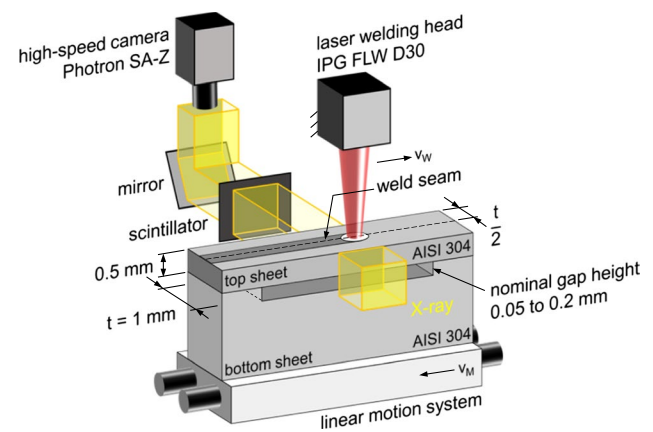
Table 1 Laser welding parameters

Parameter	Symbol	Unit and quantity
Laser beam power (cw-mode)	P_L	380 W
Wavelength	λ	1,070 nm
Focal diameter	d_f	approx. 60 µm
Fiber diameter	-	50 µm
Collimation length	-	85 mm
Focal length	-	100 mm
Focal position	z_0	Top sheet surface
Welding speed	v_W	8 m·min^{-1}

Fig. 3 Setup for high-speed synchrotron X-ray imaging

direction was aligned with the welding direction for the experiment. A rolled plate of a thickness of 1 mm was used as bottom sheet while the rolling direction was oriented perpendicular to the upper sample. A targeted manipulation of the gap size was chosen because it is known to be a key parameter for "false friend" formation. A stepwise adjustment of gap heights up to 0.2 mm in 0.05 mm steps was realized by milling the contour of the bottom sheet. The actual gap height can vary from the nominal gap height due to distortion, so for certain aspects of the analysis, a measurement was performed in the high-speed images. The movement of the sample is visualized by v_M in Fig. 3 while v_W represents the resulting welding direction.

The small sample width of $t = 1$ mm enabled a high recording rate of 100,000 Hz during the welding experiment of the AISI 304 (X5CrNi18-10/1.4301) high-alloy steel to visualize keyhole and melt pool behavior whereby the laser beam was aligned to the specimen center (t/2). Therefore, a small focal diameter was necessary to avoid heat accumulation which is why the fiber laser setup described in Section 2.1 was used for the study. The laser welding head was stationary and the sample was moved by a linear motion system allowing to keep the region of interest including the keyhole and melt pool at the same position over time. It should be noted that a constant penetration depth of approx. 300 µm into the bottom sheet was addressed in the zero-gap configuration. In order to address fundamental aspects on "false friend" formation, a partial penetration weld was carried out to limit the effect of thermal distortion during welding, i.e., to keep the focal position close to the surface of the top sheet and to stay inside the field of view of the synchrotron imaging setup. The material properties necessary for the calculation of the bond number *Bo* were taken from [26]. Values were kept constant at a temperature of 1700 °C which is above the liquidus temperature of AISI 304 [27]. The density of the surrounding atmosphere was neglected due to the high difference to the melt density.

The synchrotron experiments were carried out at the European Synchrotron Radiation Facility (ESRF) at beamline ID19. A X-ray energy ≤ 60 keV with a beam size of 4×4 mm^2 was used for the in situ high-speed recordings. A scintillator manufactured by Crytur (Ce-doped $Lu_3Al_5O_{12}$) with a thickness of 250 μm was coupled to a Photron SA-Z high-speed camera (distance to sample 4.5 m, frame rate 100,000 Hz, resolution: 512×328 pixel^2). It should be noted that the gap height affects the brightness and contrast of the image produced, as the attenuation of the X-ray intensity at the scintillator depends on the amount of material in between. In order to increase the image quality, the high dynamic range (HDR) option of the software Photron Fastcam Viewer 4 was applied to the images and a piecewise linear grey level transformation was utilized to enhance contrast and details of keyhole and melt pool. Figure 4 shows the processing carried out for a sample frame including the corresponding histograms. It should be noted that the phase contrast allowed imaging of the keyhole and the outer melt pool contour, but the solid-liquid transition within the sheets cannot be visualized. Finally, to increase the contrast at the edges, an unsharp mask was applied (radius: 1 pixel, mask weight 0.5).

3 Results and discussion

3.1 Ex situ inspection of weld seams

To get an overview of the macroscopic appearance of the weld, the "false friends" are first observed ex situ. Figure 5 shows a side view of the specimens after welding with different nominal gap heights. The photographs illustrate a section of the area with a gap and the resulting joint, i.e., it is also apparent whether the melt was able to bridge the gap. In all cases it was ensured that the penetration depth of the weld was sufficient to form a joint between both sheets — a more detailed view is provided in Section 3.2 by the synchrotron experiments. It should be noted that the lateral faces of the top and bottom sheets appear different due to the wire cut surface of the top sheet compared to the surface after rolling for the bottom sheet even if both are made of the same material (AISI 304).

A continuous weld was reached for nominal gap heights of 0.05 mm and 0.10 mm in the area shown in Fig. 5. A further increase in gap height led to the formation of "false friends," i.e., the weld was repeatedly interrupted, while a bridge between the top and bottom sheets periodically occurred in the experiment. The bridge was shorter in length as the gap height increased, which can be observed by the comparison of the nominal gap height of 0.15 to 0.20 mm. The average bridge length of the complete sample was 645 μm ± 232 μm for a nominal gap height of 0.15 mm and 347 μm ± 80 μm for a nominal gap height of 0.20 mm demonstrating the effect of the gap. The deviation of the respective values may be due to the distortion that occurs during welding and the resulting deviations between the nominal gap height and the actual value of the gap during the experiment. The actual gap is considered in the following analysis of the synchrotron experiments for this reason.

Therefore, the "false friend" obviously occurred between the bridges, i.e., in the area with a lack of fusion between both sheets. The top view of the weld did not show
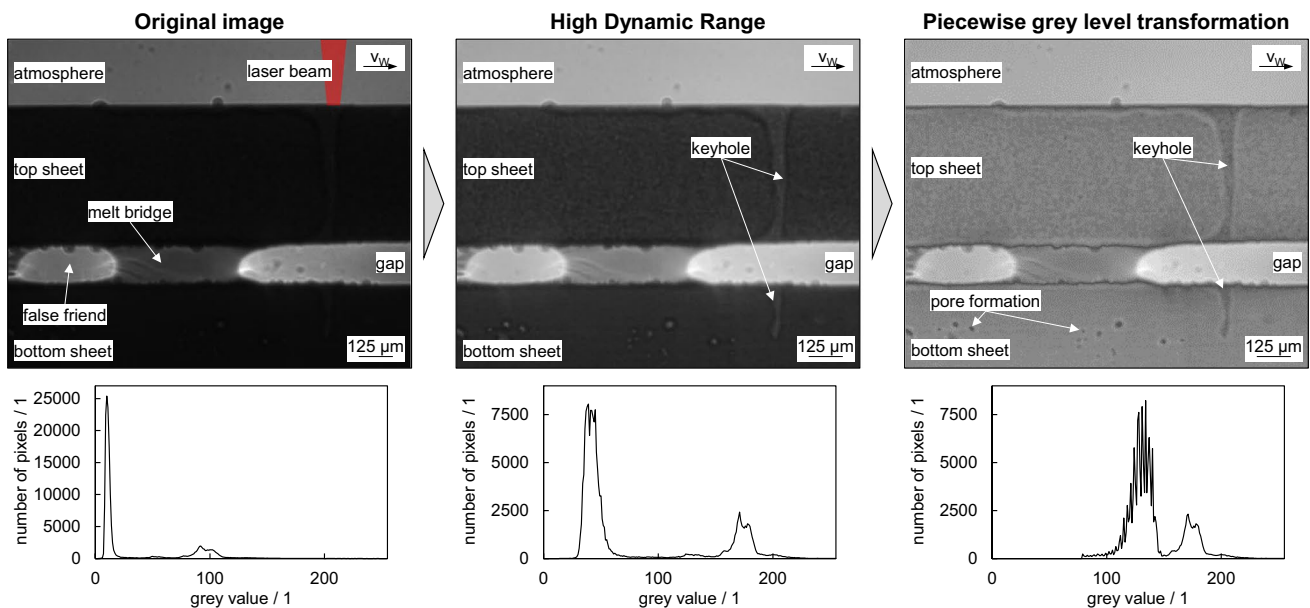

Fig. 4 Processing of high-speed X-ray images for a sample frame and related histogram
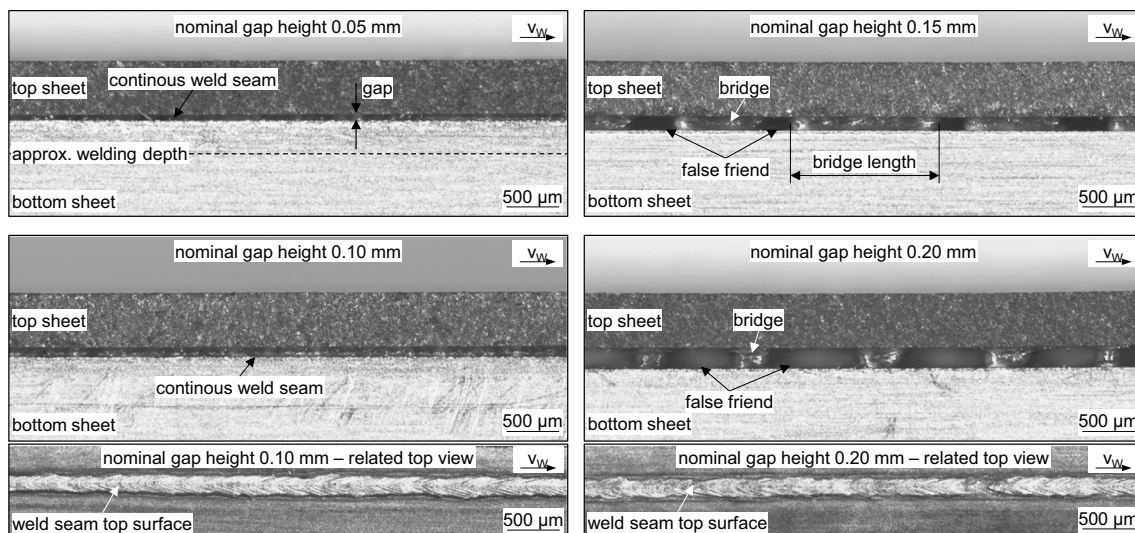
Fig. 5 Side-view of specimens for different nominal gap heights from 0.05 to 0.2 mm with corresponding weld seam top view in selected cases

significant underfill or other features that would directly indicate the presence of a weld seam defect like a "false friend" as shown in in Fig. 5 for the different gap heights of 0.10 mm and 0.20 mm. In order to understand the occurrence of discontinuities between melt bridges and the associated formation of "false friends," in situ observations were carried out during the welding process.

3.2 In situ study of weld seams

3.2.1 Formation of "false friends"

The formation of the melt bridge is described coming from the zero-gap configuration in the experiment. It can be assumed that the gap will not increase so suddenly for real parts, but rather gradually, e.g., due to distortion or insufficient clamping. In this respect, the experiment represents the worst-case scenario since a maximum gap dimension must be bridged immediately and entirely.

Figure 6 shows an image sequence from welding in a zero-gap configuration and its transition to welding with a gap including the formation of "false friends" (see Section 2.2). The exemplary image sequence is taken from a weld with a nominal gap height of 0.15 mm. It should be noted that the phenomena shown could also be reproduced for other gap heights. A time stamp has been assigned to each frame representing the time difference from the first frame displayed in zero-gap situation. The time interval was based on significant events during the process, rather than being chosen to be constant. In addition, a label (letters A-V) has been assigned to each frame to make it easier to relate each frame to the explanation in the text.

- A ($t = 0$ ms): The welding process is shown in a zero-gap configuration. The zero-gap can be seen between the top and bottom sheets, while the keyhole appears to be formed unimpeded between the two joining partners. A common melt pool is formed between both sheets and the front and rear walls of the keyhole are well visualized. The highly dynamic behavior of the keyhole is also evident in the following images and will be described in more detail when a direct impact on the phenomena in the gap is given. The melt pool can be seen from the wave formation on the top sheet surface. However, the phase contrast is not high enough to reveal the differences between the solid AISI 304 and the liquid melt pool.

- B–E ($t = 0.6\ldots3.6$ ms): The keyhole front bursts the gap and melt is ejected in the welding direction (B). The common melt pool forms a melt bridge behind the keyhole due to the surface tension (C–D). It was observed that the stochastic instabilities introduced by the burst are of minor importance compared to the trailing melt pool volume for the formation of a stable melt bridge trailing to the keyhole. The keyhole is divided into two keyholes, named keyhole 1 in the top sheet and keyhole 2 in the bottom sheet (D–E).

- F–G ($t = 4.7\ldots9.5$ ms): Solidification of the melt bridge begins at the trailing end and is well visualized in the X-ray images due to a chevron structure dividing liquid and solid phase (G). In addition, the distance between the keyhole (indicated by a dashed line in the centreline of the laser beam) and the melt bridge is increasing over time (F–G). Bridging the gap requires an equivalent volume of molten material. Since the melt volume is limited,
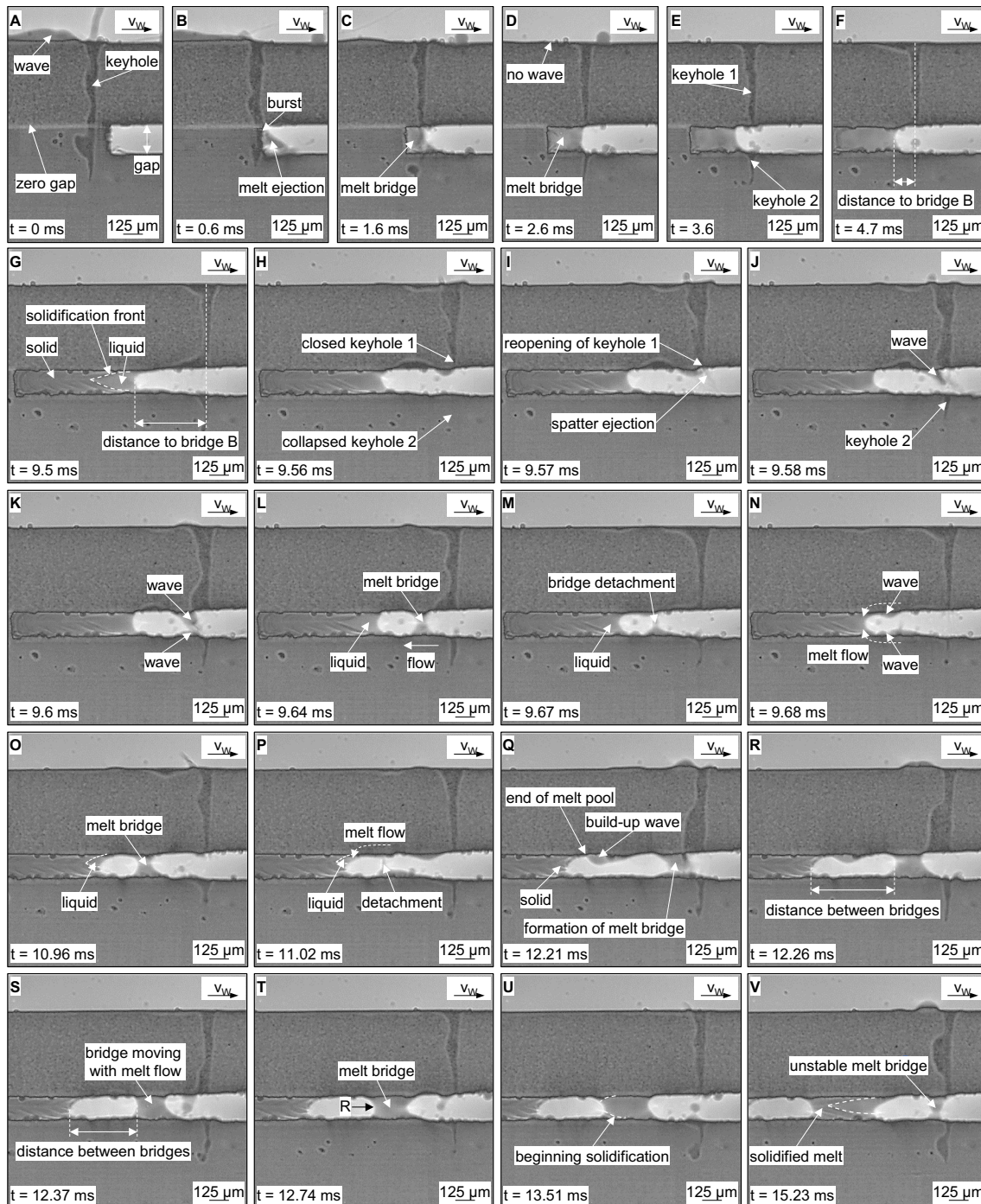
Fig. 6 Image sequence of gap bridging and false friend formation (nominal gap height = 0.15 mm)

the melt bridge cannot be fed equally and the distance between the keyhole and the melt bridge increases. A detailed description of this behavior is given for different gap heights in Section 3.2.2.

- H–K ($t = 9.56…9.6$ ms): Keyhole and melt pool dynamics cause the keyhole to close at the transition to the gap in the top sheet. At the same time, the keyhole in the

bottom sheet has already collapsed and is no longer visible (H). The abrupt opening of the bottom of keyhole 1 in the top sheet (I) leads to melt pool waves (J), which also occur with a delay in the bottom sheet due to the new formation of keyhole 2. Both waves meet (K) forming a melt pool bridge. The short timescales of these effects should be noted, as there is only about 0.04 ms

between the collapse of keyhole 1 (H) and the formation of the molten pool wave (K). It should be noted that these mechanisms may vary for different welding speeds or keyhole regimes, but the formation of melt pool waves at the rear wall of the keyhole is described in the state of the art [28], i.e., such massive instabilities as keyhole collapse may not necessarily required to form melt bridges.

- L–N ($t = 9.64…9.68$ ms): The melt bridge follows the melt flow in the backward direction (L) and quickly begins to detach (M). The remaining waves in top and bottom sheets are transported by the melt flow to the melt bridge, i.e., feeding is continued (N). However, the distance between the keyhole and the melt bridge continues to increase, indicating that the feed rate of the melt bridge is insufficient compared to the volume to be bridged, while the remaining amount of liquid material in the melt bridge continues to decrease, as indicated by the chevron structure.

- O–S ($t = 10.96…12.37$ ms): Newly formed melt bridges resulting from keyhole and melt pool instabilities are transported backwards and remain unstable, i.e., are detached (O–P). Even if the feed through the bottom melt pool has already been prevented by solidification, the flow channel in the top sheet remains and leads to the corresponding dissolution of the new melt bridge. The asymmetry in solidification and the resulting closure of the flow channels for feeding can be explained by different temperature gradients due to the surrounding volume and different energy input in the upper and lower sheet, which can already be seen from the welding depths (P). The end of solidification of the existing melt bridge is well indicated by the melt pool wave (Q) generated by the backward-oriented flow of the melt pool, and reflected at the solidification front, i.e., flowing back in the welding direction afterwards (R). A newly formed melt pool bridge (Q) continues to follow this backward flow, which can be recognized by the decreasing distance between the solid and liquid melt bridges (R–S) but is no longer detached, as the feeding of the former bridge is obstructed by the solidified channel. In addition, the build-up wave reflected at the end of the melt pool was unable to disrupt the melt bridge, indicating its stability (Q–S).

- T–V ($t = 12.74…15.23$ ms): The stable melt bridge is then completely molten and fed by the reconnected melt pool due to back-oriented flow. The radius R formed by surface tension in the projection plane is clearly visible and remains quite stable over time (T, U). Solidification starts again in the part furthest away from the keyhole and continues in the welding direction (U). Melt bridges that form in the meantime remain unstable (V) until the feed is discontinued, i.e., the melt bridge is completely solidified, and the mechanism starts again from the

beginning. It should be noted that the melt pool in the "false friend" area of the top sheet is not significantly lowered, thus hindering visual detection.

Based on these findings, two key effects could be identified to describe the "false friends." First, inadequate feeding of an existing melt bridge from the top and bottom melt pools and second, the formation and stability of newly forming melt bridges. After describing these processes through an example, the following sections discuss the two key effects in more detail with respect to the effect of the volume to be bridged, the solidification processes, and the stability of the melt bridge.

3.2.2 Formation and feeding of melt bridges

First, we will take a closer look at feeding an existing melt pool bridge from the melt pool. In Section 3.1, it was already shown from the ex situ observations that the gap has a significant influence on the formation of "false friends." In addition, the first in situ observations in Section 3.2.1 suggested that feeding is insufficient if the distance between the melt bridge and the laser beam or keyhole increases with time. In order to understand these processes better, the distance between keyhole and melt bridge was determined for different gap dimensions. The distance B was measured from the centreline of the laser beam to the maximum radius at the center of the stable melt bridge in time steps of 0.5 ms. Two aspects should be noted: Firstly, that temporary forming melt bridges are not considered for the measurements, as they will detach under the influence of melt flow and eventually contribute to the feeding of the stable melt bridge (see Section 3.2.1). Secondly, the time $t = 0$ does not correspond to the start of welding, but to the beginning of the exemplary time interval evaluated for the distance between the keyhole and the melt bridge.

Figure 7a shows the distance B between the melt bridge to the laser beam over time for different nominal gap heights of 0.10 mm, 0.15 mm, and 0.20 mm. The field of view in the synchrotron experiment resulted in a maximum measurable distance of approx. 1200 µm between the laser centreline and the melt bridge. Due to the fact that the melt bridge is already completely solidified when the maximum field of view is reached (hatched area), distances beyond were extrapolated based on the welding speed of 8 m/min. The measured gap heights are provided in associated graphs because they are changing over time due to thermal distortion and the clamping situation. In this case, the gap height is decreasing over time because the chosen time interval of 50 ms (related weld seam length: approx. 6.7 mm) was oriented towards the clamping element while the gap height before was already increased by thermal distortion. The method was chosen to represent the changing conditions while maintaining comparability under different nominal gap heights.
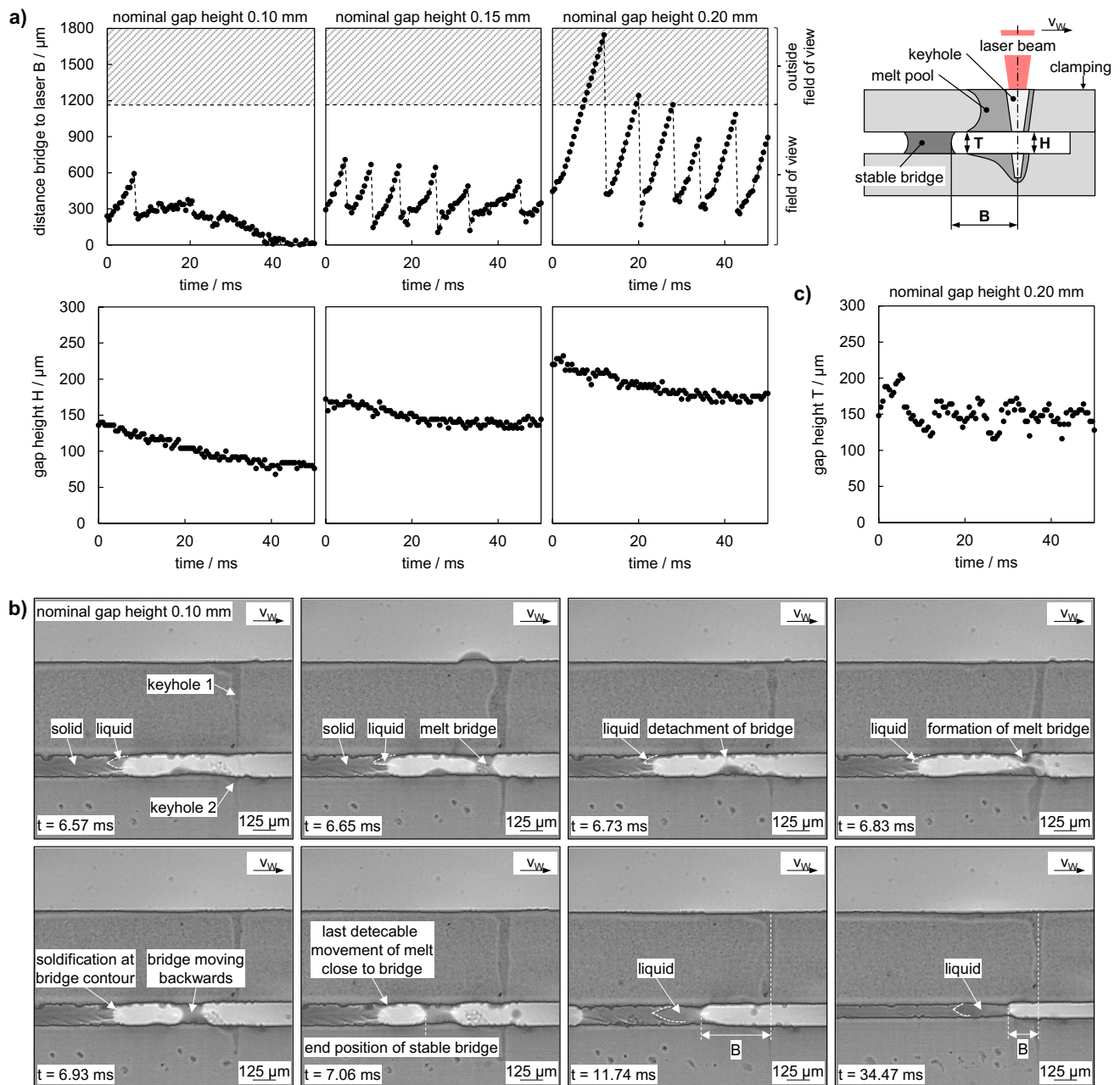
Fig. 7 a Distance between stable melt bridge and laser beam and related gap height H over time, **b** exemplary image sequence from nominal gap height 0.10 mm, **c** gap height T over time for a nominal gap of 0.20 mm

Starting with a nominal gap height of 0.10 mm, it is apparent that the distance B is increasing up to 600 µm and then dropping to 300 µm which is indicating the presence of a "false friend" as seen in the image sequence before. The distance then increases slightly (up to a time of approx. 20 ms) due to the need to feed the gap. Subsequently, the distance B continues to decrease due to the overall reduced gap height H. When H reaches approx. 80 µm, the bridge is directly behind the keyhole (approx. 40 ms). As a result, no further "false friends" are formed. It should be noted that

the appearance of the "false friend" is again related to the solidification of the flow channel toward the melt bridge. Therefore, Fig. 7b shows an image sequence with time points corresponding to the plots in Fig. 7a. A large distance B between the melt bridge and the laser beam centreline can be seen at initial time depicted ($t = 6.57$ ms). The melt bridge has already solidified to a large extent. As the time increases new melt bridges are formed, but they continue to detach due to the melt flow as the solidification within the melt bridge is not yet completed ($t = 6.65\ldots6.73$ ms), i.e.,

the distance B is still measured to the existing stable bridge. When the solidification front reaches the end of the existing stable melt bridge, a newly formed bridge remains stable. This new bridge moves with the melt flow against the welding direction ($t = 6.83…6.93$ ms). The last detectable movement in the transition area from the preceding bridge to the top sheet is seen when the new melt bridge reaches its end position ($t = 7.06$ ms). The bridge continues to be stable, and the distance B follows the gap height over time, exemplarily shown for $t = 11.74$ ms and $t = 34.47$ ms.

In comparison, at the nominal gap height of 0.15 mm, the distance B from the melt bridge to the laser beam increases significantly from the time of observation onwards ($t = 0$ ms) and reaches values up to 708 μm. This behavior is repetitive and can be observed about 7 times in the 50 ms interval. This indicates that the melt bridge feed is insufficient to fill the gap and the mechanisms described in Section 3.2.1 for the formation of "false friends" occur repeatedly. The gap height H also decreases over time due to welding in the clamping direction, which also affects the decreasing distances B between the laser beam and the melt bridge. For a gap height of 0.20 mm, the behavior becomes even more pronounced, i.e., the distances B between the melt bridge and the laser beam become even larger and reach over 1700 μm for the largest gap dimension in the time interval considered. Again, the distance B tends to follow the gap height H, i.e., as the gap gets smaller, the distance decreases. The large distances B already indicate that at very large gap heights there is insufficient feeding from the melt pool into the bridge. This is consistent with the observations in Section 3.1 as the shortest bridge length was determined for the largest nominal gap height. Larger gap heights also hinder the formation of new melt bridges. This can be seen when considering the maximum gap height T to be bridged in the rear area of the melt pool (see Fig. 7c). The evaluated images and time points correspond to Fig. 7b. The values of the gap height T fluctuate periodically, which is contrary to the progression of the corresponding gap height H leading to the laser beam. Since the gap height T varies significantly over time compared to the steady change in gap height H, it cannot be attributed to distortion or shrinkage of the solidified weld.

Figure 8 shows an image sequence with time points corresponding to Fig. 7c. The initial situation at $t = 3.41$ ms depicts the partially solidified melt bridge and a clearly visible keyholes in top and bottom sheet for a quite large gap height of approx. 220 μm. Extending the previous considerations, a significant mass transfer between the melt pools in the top and bottom sheet can be observed. On the one hand, due to melt pool instabilities, i.e., waves and spatters, which would have led to the formation of a melt pool bridge in the case of smaller gaps ($t = 3.46$ ms, $t = 4.71$ ms). On the other hand, if melt pool bridges are formed, they remain unstable and detach after a very short

time ($t = 3.78$ ms). Both aspects together lead to a significant increase in melt pool volume in the bottom sheet as clearly detectable for $t = 5.78$ ms. It should be noted that in some cases small melt pool waves or spatter may form thin bridges which are unstable due to the small total volume or due to the flow dynamics in the overflow melt pool of the lower sheet.

The enlarged melt pool will begin to solidify as the time increases, resulting in a reduction of the gap height T in this area ($t = 7.02$ ms). Due to the small dimensions in the edge region, the onset of solidification can be followed primarily by the movement of the melt pool ($t = 7.02$ ms). Over time, the solid-liquid transition can be clearly seen from the solidification front ($t = 12.12$ ms). Material continues to accumulate in this area as a result of melt pool movement and subsequent solidification. Dynamic events in the welding process continue to cause material transfer from the upper to the lower melt pool. Instabilities, such as the closing of keyhole 1 in the top sheet and the correlated collapse of keyhole 2 in the bottom sheet ($t = 12.12$ ms) followed and its abrupt re-opening of keyhole 1, result in a significant melt pool wave ($t = 12.13$ ms). The re-formation of keyhole 2 in the bottom sheet also leads to the formation of a melt pool wave, supported by the melt displacement induced by the extensive keyhole bulging ($t = 12.15$ ms). The collision of the two waves creates a new melt pool bridge, which moves in the direction of the reduced gap due to the backward-oriented flow. The occurring inertia forces when reaching the end position at high velocities do not result in the separation of the bridge even when a significant deformation can be observed ($t = 12.47$ ms). The reduced gap T at the solidification front allows the bridge to stay in place due to the surface tension. This behavior demonstrates that the drag forces are smaller than the cohesion forces due to surface tension in this case. The bridge stabilizes in its position and is fed from the melt pool ($t = 13.30$ ms). The large gap height and progressing solidification cause the bridge to quickly freeze again and the mechanisms described are repeated at intermittent intervals. The results clearly indicate the effect of the gap height and surface tension on the formation and stability of melt bridges; hence, this aspect will be discussed in the following section.

3.2.3 Stability of newly formed melt bridges

The melt flow affects the formation of melt bridges, i.e., if a previously formed melt bridge is still being fed, the melt bridge will detach (see Sections 3.2.1 and 3.2.2). After solidification of the flow channels into the melt bridge, which in many cases is identical to complete solidification of the bridged zone, a new melt bridge can form. This procedure is then dominated by the cohesion forces, i.e., the surface
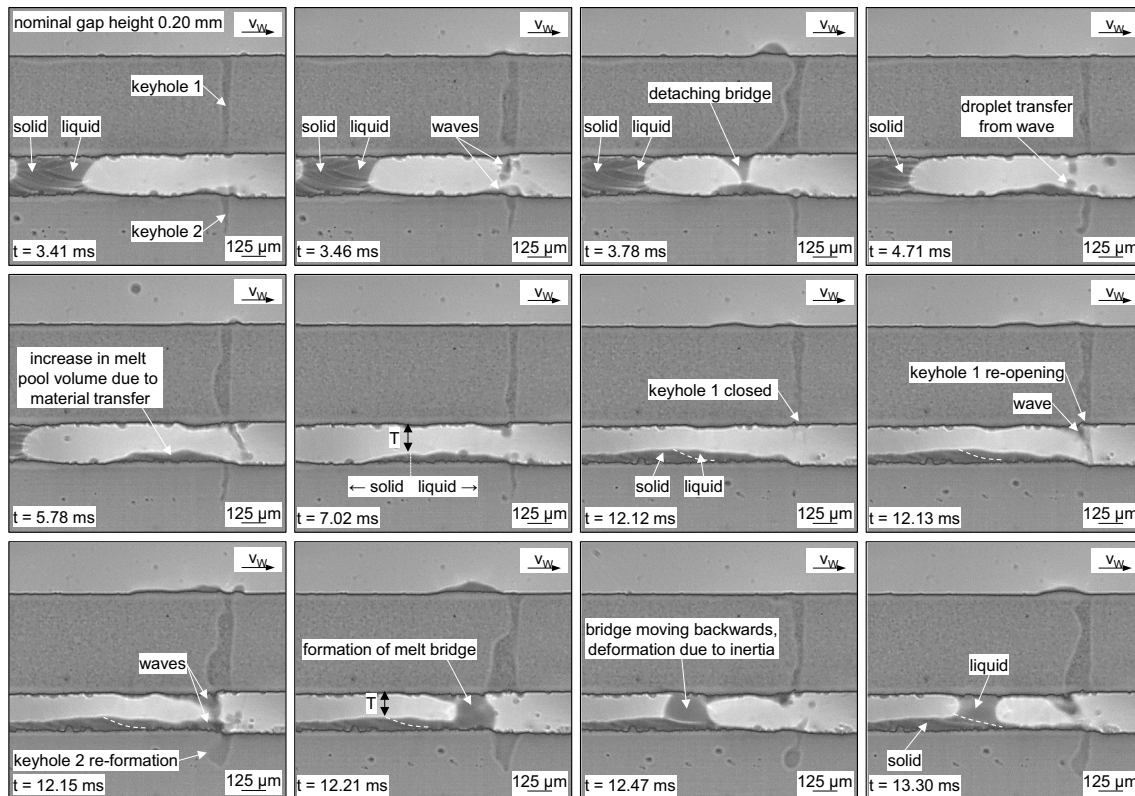
Fig. 8 Image sequence for gradual change in gap height due to solidification of the bottom sheet melt pool (nominal gap height: 0.20 mm)

tension, compared to the drag forces (see 3.2.2). Under these conditions, the stability of the melt bridge can be described by the bond number Bo (see Eq. 1) and the actual gap height T.

Figure 9a shows the gap height T and the correlating bond number Bo for stable (○) and unstable (●) melt bridges. Stable melt bridges mean that no detachment has occurred after their formation, whereas unstable bridges have separated. Forming melt bridges were considered for all different nominal gap heights where false friends occurred. The dimensions gap height T and radius R of the melt bridge are taken from single frames at different times over the entire weld, i.e., the quasi-stationary conditions of the bond number Bo as used in other cases cannot be achieved here. It should be noted that firstly, for stable bridges, a quasi-stationary state is established, well recognizable by the residual radius of the melt bridges even after solidification and is therefore not considered critical. Unstable bridges show a more pronounced fluctuation of the dimensions, but in many cases, there is a time interval between formation and collapse which is clearly defined by the surface tension due to its appearance. In this case, measurements are obtained. These aspects will be discussed below using appropriate sequences of images.

In general, the relationship is that of an exponential function passing through the origin where four ranges occur.

Range I extend from the origin of the graph to the formation of stable melt bridges from approximately up to bond number Bo of approx. 95. The origin of the graph is taken into account because for a gap of zero height, the radius and therefore the bond number Bo would also be zero. Figure 9b (I — zero gap) shows a corresponding image with zero gap and a single keyhole and a leading melt pool. In addition, continuous melt bridges, i.e., after the transition from the zero gap to the nominal gap (see 3.2.1), have not been considered. The gap leads to a separation of the keyhole in top and bottom sheet and the gap is bridged trailing to the keyhole. The gap heights and radii would fit along the dashed line of the curve, but there are no new bridges forming to consider (see Fig. 9b, I — continuous melt bridge).

Range II covers the interval where stable melt bridges are formed and bond numbers Bo between approx. 95 and 260. It is important to note that these Bo and corresponding gap heights allow new bridges to be formed in a stable manner — but at the same time, deficient feeding of previous bridges causes them to be formed. Therefore, "false friends" are created from this area onwards. Figure 9b (II — Bo = 212) shows a stable melt bridge formed in this range with the neighboring "false friend" and the measured radius R.

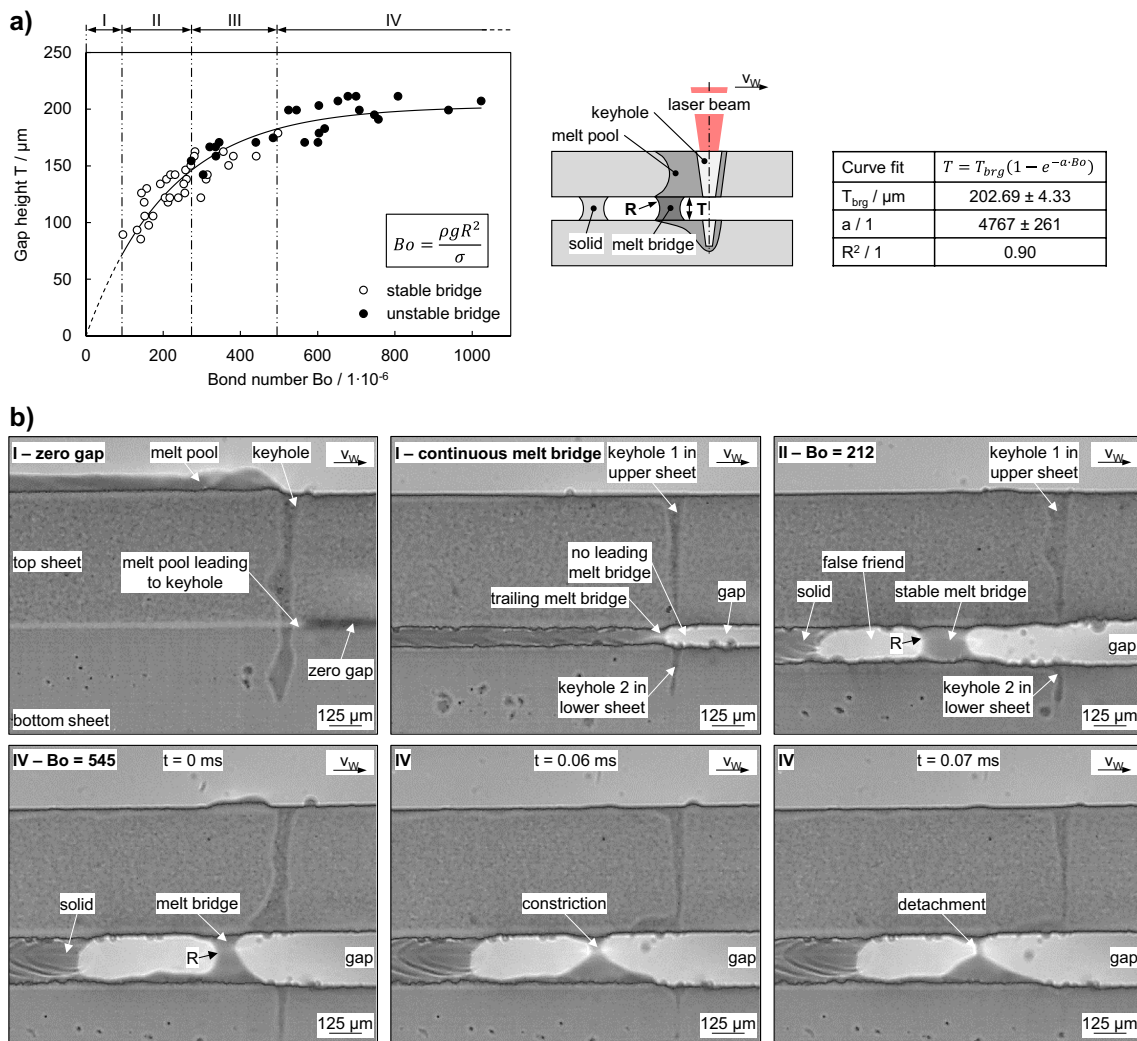Range III marks a transitional interval where stable and unstable bridges occur parallelly (Bo = 260...480). The

Fig. 9 a Description of melt bridge stability for newly formed bridges depending on gap height T and Bond number (Bo), **b** corresponding images for selected ranges and Bond numbers (Bo)

unstable bridges in this area are predominantly characterized by large gap heights leading to the laser beam. In this case, bridging requires mass transfer from the upper to the lower melt pool and the subsequent solidification which reduces the actual gap height T (see 3.2.2). If bridges are formed due to smaller melt pool waves or spatter, these are mostly very thin and unstable. If larger waves create bridges, then these are mostly stable. Variations in the radii for comparable gap heights result in different bond numbers Bo, which might be explained by different temperature-time profiles, e.g., the occurrence of melt bridges depends on instabilities in the melt pool and keyhole which are not strictly periodic or melt accumulation in the bottom sheet leads to changing temperature gradients. Therefore, the melt temperature may vary and result in different surface tension values, which are assumed to be constant in this paper.

In range IV, for bond numbers above approx. 480, no stable bridges are formed. Figure 9b (IV — Bo = 545)

shows the formation of a melt bridge where a radius R can be determined in a time frame where the surface tension appears to be dominant ($t = 0$ ms). However, the melt bridge is starting to detach with increasing times ($t = 0.06...0.07$ ms). It can be assumed that the gravitational force acting on a melt bridge rises with increasing melt bridge mass and thus with increasing gap height. At the same time, mass transfer between the top and bottom sheet is observed, based on the asymmetric detachment of large, unstable melt bridges. However, additional phenomena that cannot be observed in this study, such as changes in the inner melt pool flow with increasing gap height, can also influence fluctuations and thus bridge detachment. This behavior should be kept in mind when discussing the radii measured at individual frames, i.e., conditions are not stable in these cases. However, the data match up well and indicate the largest gap that can

be bridged on a temporary basis T_{brg}. This value is taken into account accordingly in the fit of the curve.

It should be noted that the borders between Bond numbers Bo and gap heights are not distinctive and determined for this specific setup. However, it seems to provide valid descriptions of the fundamental effects for the "false friend" formation. Further investigations can address different focal diameters, sheet thicknesses or welding speeds to provide additional information on the generally validity of the descriptions given. In addition, the effect of surface tension can be considered by using shielding gases to protect the melt pool from atmospheric oxygen to provide further information on melt bridge stability in the context of bond number Bo.

3.2.4 Model concept for "false friend" formation

The findings on the relevant phenomena for the formation of "false friends" can be summarized in a model concept, consisting of four phases (see Fig. 10). Phase I represents an existing bridge consisting of liquid material fed by the melt pool. The origin of this melt pool bridge is irrelevant, i.e., it can be caused by the transition of the welding process from a zero gap to a gap from a common melt pool, or by the formation of a melt bridge between two separate melt pools in the top and bottom sheets.

Phase II shows that, depending on the gap height, the feeding of the melt bridge is limited because there is not enough melt volume available to form a permanent bridge. This means that the distance B between the laser beam and the melt bridge increases over time. It can be assumed that the solidification front and the increasing distance therefore result in a continuous reduction of the flow channel cross-section for feeding, which also increases the fluid drag due to the cooling and the related increase in viscosity [29] as seen for comparable materials based on different positions in the melt pool [30]. When the flow channel solidifies, feeding is eventually terminated. This process can be asymmetric between the top and bottom sheets depending on melt pool geometries, but no stable melt bridges are formed due to melt pool dynamics as long as a flow channel is present. It should be noted that the penetration depth

of the weld seam is comparable due to the presence of the keyhole in the bottom sheet.

Phase III begins after the flow channels have solidified. Depending on the actual gap height T trailing to the keyhole, may influenced by material transfer between both melt pools and its solidification in the gap area, new melt bridges can form due to process instabilities caused by keyholes and melt pool. Bridges form behind the keyhole and are moving backwards until the end of the melt pool is reached. The stability of the bridges is described as a function of the bond number Bo and the actual gap height T, i.e., the cohesion force based on surface tension is the leading mechanism for keeping newly formed bridges stable under these conditions.

In phase IV, the melt bridge begins to solidify while feeding continues through the upper and lower melt pools. The "false friend" is created between the previous and the new, now solidifying, melt bridge. The feed depends on the gap height, and if the gap is too large, the phase I state will be reached again over time.

Finally, the effect of conduction mode and deep penetration welding on the formation of "false friends" is briefly discussed. It should be noted that the occurrence of "false friends" needs the ability to bridge a gap while the melt pools in the top and bottom sheets are separated. Conduction mode welding of lap joints requires the presence of heat conduction between both sheets. If a certain gap occurs, the melt pool in the top sheet will remain due to absorption of the laser beam at its surface, while the amount of melt in the bottom sheet will decrease until it is completely solidified due to insufficient heat and mass transfer. In addition, dynamic events in conduction mode welding are limited because of the absence of a keyhole. Thus, occurring gaps cannot be bridged again and both sheets continuously separate due to the lack of fusion without forming "false friends." In deep penetration welding of lap joints, the presence of a keyhole in each of the top and bottom sheets results in the formation of two separate melt pools over a large gap height, i.e., no contact between both sheets is required for sufficient energy input in the bottom sheet. These two separate keyholes and melt pools lead to dynamic events, such as waves and spatters, which are required to form new melt bridges and result in the entrapment
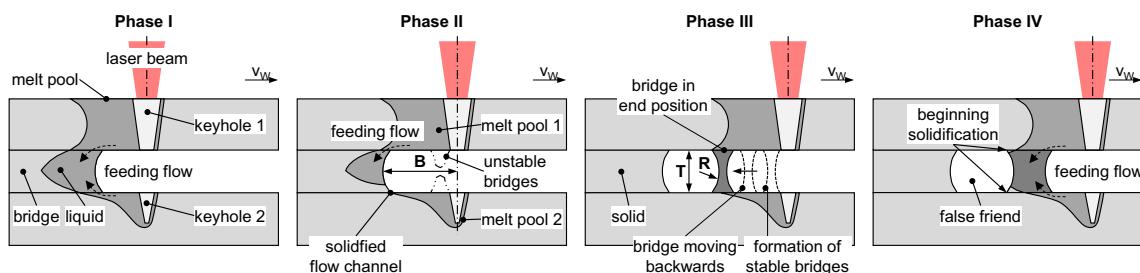

Fig. 10 Model concept for "false friend" formation

of areas of lack of fusion in the interface, thus forming "false friends".

4 Conclusion

The article provides a detailed description to the formation of "false friends" in laser beam welding based on high-speed synchrotron x-ray imaging. The studies were performed on AISI 304 high-alloy steel using a fiber laser with a focal diameter of 60 μm and a welding speed of 8 m/min. The configuration, combined with a sheet width of 1 mm for X-ray imaging, allowed to obtain high acquisition rates. An acquisition rate of 100 kHz enabled the time-dependent visualization of keyhole behavior, melt pool fluctuations, and gap solidification processes. For the first time, the phenomena of "false friend" formation have been the subject of holistic observation and description.

Based on ex situ observations on the occurrence of "false friends" in relation to different gap heights, in situ experiments were performed. In this way, the feeding of the melt bridge via the melt pool, the central influence of the solidification of the feed channel on the stability of newly formed melt bridges, and their correlation with surface tension and gap height could be determined. In addition, the significant impact of process instabilities on the formation of new melt bridges, such as keyhole closure or collapse, has been shown. Finally, the results were holistically described by a model concept.

Further investigations on the side of the laser beam process will include different focal diameters, sheet thicknesses or welding speeds to provide additional information on the generally validity of the descriptions given. Additional insights on the side of the materials will address the effect of surface tension by using shielding gases, e.g., to protect the melt pool from atmospheric oxygen. The novel insights into the phenomena of "false friend" formation can also support the development of new monitoring techniques for detecting such hidden defects, e.g., based on acoustic process emissions.

Data Availability The data used in this study are available upon request from the corresponding author.

Declarations

Conflict of interest The authors declare no competing interests.

References

1. Deepak JR, Anirudh RP, Saran Sundar S (2023) Applications of lasers in industries and laser welding: a review. Materials Today: Proceedings. https://doi.org/10.1016/j.matpr.2023.02.102

2. Dimatteo V, Ascari A, Fortunato A (2022) Experimental investigation on the effect of spot diameter on continuous-wave laser welding of copper and aluminum thin sheets for battery manufacturing. Optics Laser Technol 145:107495. https://doi.org/10.1016/j.optlastec.2021.107495

3. Schricker K, Drebing A, Seibold M, Bergmann JP (2022) Laser-assisted joining of AISI 304 thin sheets with polymers. Procedia CIRP 94:531–536. https://doi.org/10.1016/j.procir.2020.09.177

4. Grabmann S, Kriegler J, Harst F, Günter FJ, Zaeh MF (2022) Laser welding of current collector foil stacks in battery production–mechanical properties of joints welded with a green high-power disk laser. Int J Adv Manuf Technol 2571–2586. https://doi.org/10.1007/s00170-021-07839-0

5. Haddad E, Chung WS, Katz O, Helm J, Olowinsky A, Gillner A (2022) Laser micro welding with fiber lasers for battery and fuel cell based electromobility. J Adv Join Process (5). https://doi.org/10.1016/j.jajp.2021.100085

6. Arivazhagan N, Singh S, Prakash S, Reddy GM (2011) Investigation on AISI 304 austenitic stainless steel to AISI 4140 low alloy steel dissimilar joints by gas tungsten arc, electron beam and friction welding. Mater Des 32:3036–3050. https://doi.org/10.1016/j.matdes.2011.01.037

7. Gu H (2010) Laser lap welding of zinc coated steel sheet with laser-dimple technology. J Laser Appl 22:3. https://doi.org/10.2351/1.3485596

8. Bastuck M, Herrmann H-G, Wolter B, Zinn P-C, Zaeh R-K (2015) Acoustic in-process monitoring of laser welding, ICALEO® 2015: 34th International Congress on Laser Materials Processing, Laser Microprocessing and Nanomanufacturing 601. https://doi.org/10.2351/1.5063193

9. Nelissen G (2017) Formed metal fuel cell bipolar plates. ECS Trans 80:435–444. https://doi.org/10.1149/08008.0435ecst

10. Heller K, Kessler S, Dorsch F, Berger P, Graf T (2015) Robust "false friend" detection via thermographic imaging, Proceedings of Lasers in Manufacturing Conference: Macro Processing: Joining (Welding, Brazing), Munich, 22–25

11. Kuhl M, Mickel P-M (2009) The possibilities of and limits to detecting incomplete fusion via in-process monitoring in the case of laser welding. 2009 IEEE Conference on Emerging Technologies & Factory Automation. https://doi.org/10.1109/ETFA.2009.5347201

12. Dorsch F, Braun H, Keßler S, Pfitzner D, Rominger V (2012) NIR-camera-based online diagnostics of laser beam welding processes. Proc. SPIE 8239, High Power Laser Materials Processing: Lasers,

Beam Delivery, Diagnostics, and Applications 82390T. https://doi.org/10.1117/12.908646

13. Knaak C, von Eßen J, Kröger M, Schulze F, Abels P, Gillner A (2021) A spatio-temporal ensemble deep learning architecture for real-time defect detection during laser welding on low power embedded computing boards. Sensors 21(12):4205. https://doi.org/10.3390/s21124205

14. Kaplan A, Powell J (2011) Spatter in laser welding. J Laser Appl 23(3):032005. https://doi.org/10.2351/1.3597830

15. Rack A, García-Morena F, Schmitt C, Betz O, Cecilia A, Ershov A, Rack T, Banhart J, Zabler S (2010) On the possibilities of hard X-ray imaging with high spatio-temporal resolution using polychromatic synchrotron radiation. J Xray Sci Technol 18(4):429–441. https://doi.org/10.3233/XST-2010-0273

16. Di Michiel M, Merino JM, Fernandez-Carreiras D, Buslaps T, Honkimäki V, Falus P, Martins T, Svensson O (2005) Fast microtomography using high energy synchrotron radiation. Rev Sci Inst 76:043702. https://doi.org/10.1063/1.1884194

17. Schricker K, Schmidt L, Friedmann H, Diegel C, Seibold M, Hellwig P, Fröhlich F, Bergmann JP, Nagel F, Kallage P, Rack A, Requardt H, Chen Y (2022) Characterization of keyhole dynamics in laser welding of copper by means of high-speed synchrotron X-ray imaging. Procedia CIRP 111:501–506. https://doi.org/10.1016/j.procir.2022.08.079

18. Sevchik S, Le-Quang T, Meylan B, Farahani FV, Olbinado MP, Rack A, Masinelli G, Leinenbach C, Wasmer K (2020) Supervised deep learning for real-time quality monitoring of laser welding with X-ray radiographic guidance. Sci Rep 10:3389. https://doi.org/10.1038/s41598-020-60294-x

19. Chen Y, Clark SJ, Leung CLA, Sinclair L, Marussi S, Olbinado MP, Boller E, Rack A, Todd I, Lee PD (2020) In-situ synchrotron imaging of keyhole mode multi-layer laser powder bed fusion additive manufacturing. Appl Mater Today 20:100650. https://doi.org/10.1016/j.apmt.2020.100650

20. Zhao C, Guo Q, Li X, Parab N, Fezzaa K, Tan W, Chen L, Sun T (2019) Bulk-explosion-induced metal spattering during laser processing. Phys Rev X 9:021052. https://doi.org/10.1103/PhysRevX.9.021052

21. Hotta K, Takeda K, Iinoya K (1974) The capillary binding force of a liquid bridge. Powder Technol 10:231–242. https://doi.org/10.1016/0032-5910(74)85047-3

22. Bezdenejnykh NA, Meseguer J, Perales JM (1992) Experimental analysis and stability limits of capillary liquid bridges. Phys Fluids A 4:677–680. https://doi.org/10.1063/1.858286

23. Wilden J, Bergmann JP, Reich S, Möller L, Goecke S-F (2006) Set of a high power diode laser in order to enhance wettability conditions and process speed in a controlled short arc brazing process of zinc coated steels. ICALEO® 2006: 25th International Congress on Laser Materials Processing and Laser Microfabrication. https://doi.org/10.2351/1.5060788

24. Schricker K, Alhomsi M, Bergmann JP (2021) Thermal efficiency in laser-assisted joining of polymer–metal composites. Materials 13(21):4875. https://doi.org/10.3390/ma13214875

25. Graf T, Berger P, Weber R, Hügel H, Heider A, Stritt P (2015) Analytical expressions for the threshold of deep-penetration laser welding. Laser Phys Lett 12:056002. https://doi.org/10.1088/1612-2011/12/5/056002

26. Delacroix J, Piluso P, Chikhi N, Asserin O, Borel D, Brosse A, Cadiou S (2022) Measurements of liquid AISI 304L steel density and surface tension, and influence of surface-active elements at high temperatures. Steel Res Int 93:2100624. https://doi.org/10.1002/srin.202100624

27. Miyata Y, Okugawa M, Koizumi Y, Nakano T (2021) Inverse columnar-equiaxed transition (CET) in 304 and 316L stainless steels melt by electron beam for additive manufacturing (AM). Crystals 11(8):856. https://doi.org/10.3390/cryst11080856

28. Schmidt L, Schricker K, Bergmann JP, Junger C (1867) Effect of local gas flow in full penetration laser beam welding with high welding speeds. Appl Sci 10(5):2020. https://doi.org/10.3390/app10051867

29. Shapiro AH (1961) Shape and flow: the fluid dynamics of drag. Anchor Books - Doubleday & Company, Garden City New York

30. Rai R, Roy GG, Debroy T (2007) A computationally efficient model of convective heat transfer and solidification characteristics during keyhole mode laser welding. J Appl Phys 101(5):054909. https://doi.org/10.1063/1.2537587